Metal nanoplates: Smaller is weaker due to failure by elastic instability

Duc Tam Ho,[1] Soon-Yong Kwon,[2] Harold S. Park,[3] and Sung Youb Kim[1,*]

[1]*Department of Mechanical Engineering, Ulsan National Institute of Science and Technology, Ulsan 44919, South Korea*

[2]*School of Materials Science and Engineering, Ulsan National Institute of Science and Technology, Ulsan 44919, South Korea*

[3]*Department of Mechanical Engineering, Boston University, Boston, Massachusetts 02215, USA*

(Received 6 August 2017; revised manuscript received 15 October 2017; published 7 November 2017)

Under mechanical loading, crystalline solids deform elastically, and subsequently yield and fail via plastic deformation. Thus crystalline materials experience two mechanical regimes: elasticity and plasticity. Here, we provide numerical and theoretical evidence to show that metal nanoplates exhibit an intermediate mechanical regime that occurs between elasticity and plasticity, which we call the elastic instability regime. The elastic instability regime begins with a decrease in stress, during which the nanoplates fail via global, and not local, deformation mechanisms that are distinctly different from traditional dislocation-mediated plasticity. Because the nanoplates fail via elastic instability, the governing strength criterion is the ideal strength, rather than the yield strength, and as a result, we observe a unique "smaller is weaker" trend. We develop a simple surface-stress-based analytic model to predict the ideal strength of the metal nanoplates, which accurately reproduces the smaller is weaker behavior observed in the atomistic simulations.

DOI: 10.1103/PhysRevB.96.184103

I. INTRODUCTION

The failure mechanisms and the corresponding failure strength are fundamental issues in the study of the mechanical properties of materials. Usually, materials contain preexisting defects such as vacancies, dislocations, microcracks, etc. When the applied loading is sufficiently large, the defects can propagate and interact. For crystalline solids like metals, the deformation and failure mechanisms are typically governed by dislocation-mediated plasticity, which initiates around the yielding point. This yield strength, which is regarded as a material constant, exhibits significant size dependence [1,2]. For example, the yield strength of Au nanowires can be 100 times larger than that of the corresponding bulk material [3], and similarly all previous reports of nanomaterial strength have concluded that smaller is stronger [2,4–7]. The origin of the size dependence is due to the surface stress, the reduction of the number of defects in the material with decreasing dimensions, and the geometrical constraints on dislocation motion [2,8]. In the case of defect-free materials, the strength of the material is the ideal strength rather than the yield strength [9,10].

The ideal strength of materials can be obtained with the support of the elastic stability theory [9]. This theory was originally developed by Born [11], then improved by Hill and Milstein [12,13]. Because of extreme smallness, defect-free materials can now be synthesized, thus eliminating certain plastic deformation mechanisms that are seen in the corresponding bulk materials, some fundamental questions about nanomaterial failure must be resolved. Is plastic deformation still the failure mode of nanoscale materials? If not, then what is the key failure mechanism? What is the ideal strength of nanoscale materials? Without preexisting defects, is the ideal strength size dependent?

In this study, we employ atomistic simulations to investigate the mechanical failure modes and ideal strength of metal (001) nanoplates (freestanding nanofilms) under uniaxial stress along the [100] direction. Nanoplates can exhibit mechanical properties that are significantly different from those of the corresponding bulk materials. For example, the reduction of electrical and thermal conductivities [14] and negative Poisson's ratio behavior [15,16] in nanoplates have been reported. In the present work, we report that metal nanoplates fail without the occurrence of dislocation-induced plastic deformation. Instead, they fail homogeneously and globally, which is governed by elastic instability rather than dislocation-mediated yielding. Since the nanoplates fail due to elastic instability, the ideal strength rather than the yield strength defines the strength of nanoplates, and a unique "smaller is weaker" trend is observed. We note that while various studies have reported that nanostructures can be either elastically stiffer or softer than the corresponding bulk material [17], this work reports that defect-free nanostructures can be *weaker* than the corresponding bulk material. To explain the size-dependent strength behavior, we develop a simple surface-stress-based analytic model that predicts the ideal strength of nanoplates, and which is shown to be in excellent agreement with the simulation results. Overall, the present work demonstrates the important, and sometimes unexpected, connections between material stability, failure mechanisms, and strength at nanometer length scales.

II. SIMULATION METHODS

We designate the [100], [010], and [001] directions as x, y, and z directions. To model the bulk material, we applied periodic boundary conditions along the x, y, and z directions. To model the nanoplate, periodic boundary conditions were applied along the x and y directions while no periodicity is applied along the z direction to model the free surface. The lengths of the simulation box along the x and y directions are the same and they are five times larger than the z direction (the thickness direction) of the nanoplate. The interaction between atoms is described by embedded-atom-method (EAM) potential models [18–20].

*sykim@unist.ac.kr

In molecular dynamics (MD) simulations, we first increase the temperature from 0 K to a target temperature over 100 ps. Then the nanoplate was dynamically equilibrated at the target temperature under the isothermal-isobaric (*NPT*) ensemble over another 100 ps; i.e., the simulation box was allowed to move along the x and y directions to ensure a stress-free condition in the nanostructure. After the nanoplate was equilibrated at the target temperature, we applied uniaxial loading in the x direction with different strain rates ranging from 10^7 to 10^9 s^{-1}. Under this loading condition, σ_{xx} is the only nonzero stress component, whereas the others are zero; i.e., $\sigma_{yy} = \sigma_{zz} = \sigma_{yz} = \sigma_{xz} = \sigma_{xy} = 0$.

We also conducted molecular statics (MS) simulations to ensure that our results are independent of strain rate. For the MS simulations, the nanostructures were first relaxed to obtain an equilibrium configuration, after which uniaxial strain was applied along the x direction with strain increments of 0.001, and where all stress components except σ_{xx} were kept at zero; i.e., $\sigma_{yy} = \sigma_{zz} = \sigma_{yz} = \sigma_{xz} = \sigma_{xy} = 0$. A conjugate gradient (CG) energy minimization was employed, with convergence for each strain increment when the relative energy change was less than 10^{-16}. All MD and MS simulations were performed using the large-scale atomic/molecular massively parallel simulator (LAMMPS) [21], and the OVITO package was used for visualization [22].

III. RESULTS AND DISCUSSION

A. Elastic instability regime of the Au (001) nanoplate

We first illustrate the elastic instability phenomena in metal nanoplates. To do so, we conduct a number of uniaxial stress tests for a wide range of fcc metal (001) nanoplates at different temperatures ranging from 1 to 500 K. The various fcc metals we considered (Al, Ag, Au, Cu, Ni, Pd, and Pt) all demonstrated similar behavior in terms of the elastic instability, as well as the smaller is weaker trend, so we focus our discussion on Au for the remainder of this work. The interaction among the Au atoms is described by the embedded-atom-method (EAM) potential model developed by Cai and Ye [18]. Figure 1(a) presents the stress-strain and energy-strain curves of the Au (001) nanoplate with a thickness of 4.7 nm under uniaxial stress along the [100] direction. Under loading, both the stress and energy increase with increasing strain. The stress becomes maximum with the value $\sigma_{IP} = 3.02$ GPa at point I with a critical strain of $\varepsilon_I = 0.0775$. In defect-free nanomaterials such as nanowires, the stress drops sharply immediately after the maximum stress point [23,24], with a corresponding decrease in energy. However, as can be seen clearly in Fig. 1(a), the stress decrease is gradual rather than immediate, while the energy continues to increase. Note that the slope of the stress-strain curve is zero at the point of maximum stress, which implies that the effective Young's modulus of the nanoplate is zero at point I. If larger strains are applied to the nanoplate, the stress continues to decrease and finally drops sharply immediately after point Y.

The strain at point I can be regarded as the critical strain at which the nanoplate loses its elastic stability. We plot the configurations of the nanoplate at some important points in Fig. 1(b). We show only atoms with a centrosymmetry parameter greater than 1.0 in order to detect any planar defects like dislocations. Interestingly, at $\varepsilon = 0.082$, which is larger than ε_I, no dislocations nor any other defects are observed in the nanoplate, where the configuration appears similar to that at the initial state. This indicates that the nanoplate deforms homogeneously and globally, which is in contrast to the dislocation-mediated plasticity typically observed in other metal nanostructures such as nanowires [25]. The dislocation-free configuration is still observed in the nanoplate until the energy drops at point Y. As shown in Fig. 1(b), plastic deformation can be observed in the nanoplate as the strain becomes larger than $\varepsilon_Y = 0.0884$. Then why does a yielding event not happen immediately after the maximum stress point I? The question will be discussed in the next section.

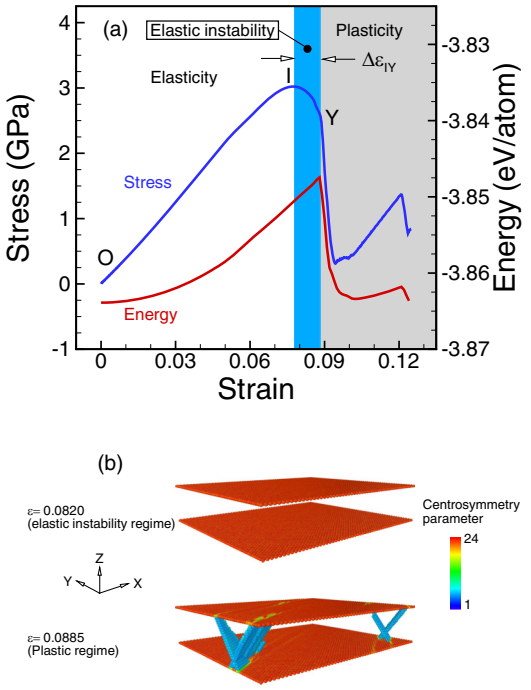

FIG. 1. Mechanical response of the Au (001) nanoplate with a thickness of 4.7 nm under the uniaxial stress condition along the [100] direction at 1 K. (a) Stress-strain and energy-strain curves. (b) Configurations of the nanoplate at different values of strain. It is clear that one more mechanical regime, elastic instability, occurs between elasticity and plasticity. In the elastic instability regime, the material deforms homogeneously without dislocation motion.

B. Elastic instability: Nanoplate versus bulk

Before discussing the failure mechanism of the nanoplate further, we first discuss the failure of the corresponding bulk material. Under uniaxial stress along the [100] direction, perfect fcc bulk materials usually fail with a homogeneous and global deformation instead of a local deformation related to the yielding mechanism. The failure is the result of the elastic instability rather than plasticity. The elastic stability theory was originally developed by Born [11] and then improved by Hill and Milstein [13] and others [26,27]. According to the theory, a material under loading is stable if and only if $\det|\overline{\mathbf{B}}| > 0$ where $\overline{\mathbf{B}} = 1/2(\mathbf{B} + \mathbf{B}^T)$ and $\mathbf{B}$ is the elastic stiffness matrix

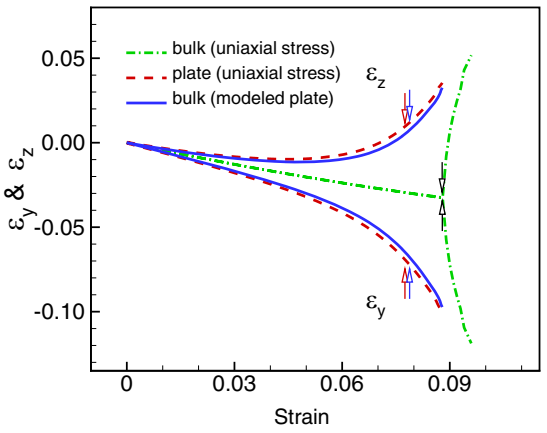

FIG. 2. Change of the lateral strains of bulk Au and an Au (001) nanoplate under uniaxial stress loading at 1 K. The arrows indicate the points at which the materials lose their elastic stability. Under the uniaxial stress condition, there is sudden contraction and expansion of the material along the lateral directions at a critical strain. Under the multiaxial loading condition (modeled nanoplate), the sudden contraction and expansion is replaced by a gradual branching. The mechanical response of the nanoplate under uniaxial stress is similar to that of the modeled nanoplate.

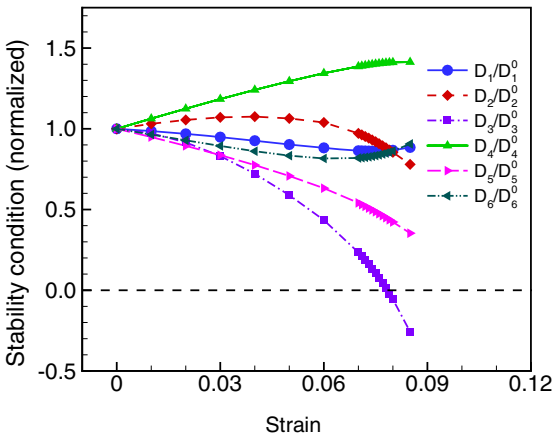

FIG. 3. Change of the elastic moduli combinations with applied strain for the Au (001) nanoplate with a thickness of 4.7 nm at 1 K. D_i^0 is the elastic combination i at the unstrained state. The elastic moduli combination D_3 reaches zero at the strain at which the stress of the nanoplate becomes maximum.

that is the combination of elastic moduli $\mathbf{C}$ and external loading τ_{ij} [26,28], as defined in Eq. (A2) in the Appendix. When $\det|\overline{\mathbf{B}}| = 0$, the material becomes unstable and deforms with an eigenstate. One can obtain the eigenstate by solving an eigenvalue problem: $(\overline{\mathbf{B}} - \lambda\mathbf{I})\mathbf{x} = \mathbf{0}$. For a bulk fcc material under uniaxial tensile stress along the [100] direction, the stability condition is simplified to four explicit stability conditions in which $C_{22} - C_{23} > 0$ is the dominant stability condition, where $\mathbf{C}$ is the elastic modulus matrix of the structure [13]. Details of the explicit stability condition for bulk fcc under uniaxial stress along the [100] direction can be seen in the Appendix. At the onset of instability, the material loses its elastic stability with an eigenstate $(\delta\varepsilon_1,\delta\varepsilon_2,\delta\varepsilon_3,\delta\varepsilon_4,\delta\varepsilon_5,\delta\varepsilon_6) = (0,-1,1,0,0,0)$, which represents a phase transformation from a tetragonal to orthorhombic structure. We note that the analysis in this study is different from the analysis of instability of nonuniform loading [29,30] and preexisting defect materials [31,32]. In these cases, the stress is nonhomogeneous across the material and thus can create local volumes that are elastically unstable. As a result, the eigensolution is more complicated [31].

We conduct a simulation involving the uniaxial stress along the [100] direction for bulk Au at 1 K and plot the change of lateral strains in Fig. 2. The lateral strains gradually decrease the same amount as the applied strain increases. However, at the critical strain $\varepsilon = 0.088$, it is clear that the lateral strains change significantly, i.e., ε_y decreases whereas ε_z increases, and the decrease in ε_y is almost the same as the increase in ε_z. In other words, a phase transformation from tetragonal to orthorhombic occurs in the material. We confirm that at the onset of the phase transformation, the stress becomes a maximum and the elastic stability condition $C_{22} - C_{23} > 0$ is violated (see Fig. 9 in the Appendix).

We now turn back to the nanoplate. As can also be seen in Fig. 2, the change of lateral strains of the nanoplate under the uniaxial stress condition is significantly different from that of the bulk material under the same loading condition. While ε_y always decreases with the increase of the applied strain, ε_z decreases initially, then increases with the increase of applied strain. As a result, an interesting phenomenon is observed in the metal nanoplate: negative Poisson's ratio along the thickness direction [15,16]. Under uniaxial stress along the [100] direction, the nanoplate has orthorhombic symmetry, rather than tetragonal symmetry as in the case of the bulk counterpart. Therefore, the stability condition for the nanoplate is more complicated. We present all the elastic stability conditions for the nanoplate under the uniaxial stress condition in the Appendix. As shown in Fig. 3, one of the elastic moduli combinations, D_3, reaches zero at the point where the stress becomes a maximum. This indicates that the nanoplate loses its elastic stability and thus it cannot stand larger stress. As shown in Eq. (A18) in the Appendix, the vanishing of D_3 leads to the vanishing of the effective Young's modulus of the nanoplate, which is why the Young's modulus is zero at point I [Fig. 1(a)]. The pairs of the black and red arrows in Fig. 2 mark the critical points at which the stresses are the maximum for the bulk material and the nanoplate, respectively. As mentioned earlier, both the bulk material and the metal nanoplate fail with global deformation; i.e., no local plastic deformation mechanisms are observed. Furthermore, while bulk Au fails via the tetragonal to orthorhombic phase transformation, there is no such phase transformation in the metal nanoplate. The lateral strain ε_y still decreases and ε_z still increases with the applied strain.

We summarize in Table I the comparison between the elastic instability characteristics of the fcc bulk and nanoplate under the uniaxial tensile loading along the [100] direction. The two cases share some similarities because both of them fail by elastic instability. For example, the stress is maximum at the onset of instability; the deformation mode at the onset of instability is defect-free deformation. In the case of the nanoplate under uniaxial stress along the [100] direction, it fails because the elastic moduli combination D_3 reaches

TABLE I. Comparison between the mechanical response of fcc bulk and nanoplate under uniaxial tensile loading along the [100] direction with displacement control.

	Bulk	Nanoplate
First vanished stability condition	$C_{22} - C_{23} > 0$	$D_3 = \begin{vmatrix} \bar{B}_{11} & \bar{B}_{12} & \bar{B}_{13} \\ \bar{B}_{12} & \bar{B}_{22} & \bar{B}_{23} \\ \bar{B}_{13} & \bar{B}_{23} & \bar{B}_{33} \end{vmatrix} > 0$
Eigenmode	$(0,-1,1,0,0,0)$	Complex
Atomic arrangement	Homogeneous	Homogeneous
Ideal strength	Value of stress at the onset of the instability	Value of stress at the onset of the instability
Behavior of stress at onset of the instability	Sharp change	Gradual change
Energy	Increasing continuously even when stress decreases	Increasing continuously even when stress decreases

zero (Fig. 3). We note again that the vanishing of D_3 is equivalent to the vanishing of the Young's modulus because $E_{[100]} = \frac{D_3}{\bar{B}_{22}\bar{B}_{33}-\bar{B}_{23}^2}$ [Eq. (A18) in the Appendix]. The strain at which the Young's modulus reaches zero [Fig. 1(a)] is the same at which D_3 reaches zero, indicating that the prediction of elastic stability theory is in excellent agreement with the MD simulation results. The corresponding deformation mode is similar to that in the elastic regime, i.e., a slight contraction along the y direction and a slight expansion along the z direction (Fig. 2). This deformation is homogeneous, and defect free as presented by and Hill and Milstein [13]. Both nanoplate and bulk also share another elastic instability characteristic, which is that the stress decreases at the onset of the elastic instability whereas the energy still increases. According to and Hill and Milstein, a material is said to be elastically stable if the change in the internal energy δU is larger than the change in the work done by external loading δW for all possible, arbitrary virtual infinitesimal deformation. In other words, the stability is dependent on not only elastic moduli but also external loading. In particular, $\delta U - \delta W > 0$ is the condition for stability, *not* $\delta U > 0$. Therefore, the energy can increase while the stress decreases, which was observed in previous reports [33,34]. The behavior of energy in this case is similar to that in buckling; i.e., although stress decreases after buckling, the energy still increases.

One may ask why dislocation nucleation or phase transformation is not seen in the nanoplate when the stress reaches its maximum in Fig. 1, and propose that the defect-free deformation might be due to the high strain rate in the MD simulations rather than the elastic instability. So far, the uniaxial stress loading condition using displacement control was considered, and now we considered the Au nanoplate under uniaxial stress condition along the [100] direction, but using force control instead of displacement control. For the force control MD simulations, the nanoplate was first dynamically equilibrated at 1 K before applying stress to the structure. The applied stress is increased from 0 to a target value with the rate of 0.41×10^{10} GPa/s at 1 K. Finally, in the third stage, we kept the applied stress at the target value at the same temperature for 200 ps. As shown in Fig. 4, the mechanical response of the structure with the applied stress slightly smaller than 3.02 GPa is totally different from the mechanical response of the structure with the applied stress slightly larger than 3.02 GPa in two aspects, including the relationship between the applied stress and internal stress, and the deformation mode. Firstly, the internal stress and applied stress are the same when the applied stress is 3.01 GPa indicating that the structure can sustain this applied stress; however, the internal stress is lower than the applied stress when the applied stress is 3.04 GPa indicating that the structure becomes unstable with this applied stress. Secondly,

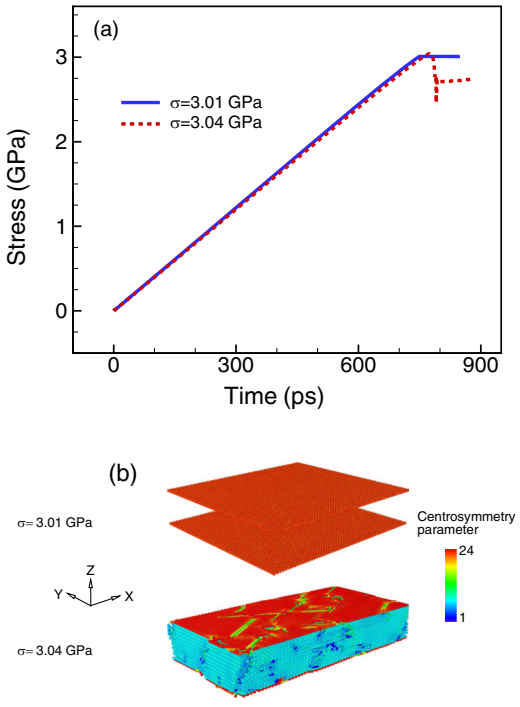

FIG. 4. Mechanical response of the Au (001) nanoplate with a thickness of 4.7 nm under the uniaxial stress condition using force control along the [100] direction at 1 K. (a) Stress-strain curves. (b) Configurations of the nanoplate at different values of applied stress. In (b), the cyan atoms in the lower configuration have hcp phase according to the adaptive common neighbor analysis. When the applied stress is slightly lower than the ideal strength of 3.02 GPa, the internal stress is the same as external stress, and defect-free deformation is observed. On the other hand, when the applied stress is slightly larger than the ideal strength of 3.02 GPa, the internal stress is lower than the external stress, and an fcc→hcp phase transformation is observed.

on the deformation mode, a fcc→hcp phase transformation is observed when the applied stress is 3.04 GPa whereas defect-free deformation is observed when the applied stress is 3.01 GPa. The two observations once again confirm that 3.02 GPa is the ideal strength of the nanoplate. The simulation results of the nanoplate under the uniaxial stress condition with the displacement control and force control agree very well with the prediction of the elastic instability. In the next paragraph, we turn back to the displacement control simulations.

Beside the similarities mentioned above, the mechanical response in the elastic regime and the elastic instability regime of the nanoplate has some significant differences from those of the bulk material. For example, in the elastic regime, the Poisson's ratio component ν_{xz} becomes negative at sufficiently large strain [15] whereas that of the bulk is positive: There is no phase transformation at the onset of the instability as in the case of bulk; the stress drop is more gradual and the dominant elastic stability condition is more complex. The difference may be explained by considering the effect of surface stress. Surface stress is known as a key parameter that leads to the large difference in mechanical properties between nanoscale materials and bulk materials [35,36]. Surface stress is associated with the reversible work per unit area needed to elastically stretch a preexisting surface, and can be expressed as $f_{ij} = \gamma\delta_{ij} + \partial\gamma/\partial\varepsilon_{ij}$ where f_{ij} is the surface-stress tensor (a second-rank tensor), γ is the surface energy density, δ_{ij} is the Kronecker delta, and ε_{ij} is the surface strain tensor [37]. For the case of isotropic surfaces, the surface stress can be rewritten as $f = \gamma + \partial\gamma/\partial\varepsilon$. The methodologies of surface-stress calculation were reported previously for surfaces at the unstrained state [38,39] and surface stress at finite strains [40]. When the surface stress is positive, i.e., the surface is under tension, and thus the surface can lower its energy by contracting. On the other hand, when the surface stress is negative, i.e., the surface is under compression, the surface can lower its energy by expanding [37]. Metal surfaces typically have a tensile surface stress, which implies that surface atoms can increase their electron density by contracting towards the bulk [41]. Consider an fcc metal (001) nanoplate having positive surface stress f, which is constrained to have its bulk lattice parameter. When removing the constraints, in order to get force balance with the tensile surface stress, the atoms in the core of the nanoplate rearrange their positions such that the in-plane stress components at the core are compressive [42], where the magnitude of the induced compressive stress is inversely proportional to the nanoplate thickness. For the nanoplates, a multiaxial stress condition of the core in the x-y plane is generated due to the relaxation induced by surface stresses [43]. We show in Fig. 5 the free-body diagram of an fcc metal (001) nanoplate.

The compressive stresses within the nanoplate core induced by the surface stresses can be shown to stabilize the nanoplate during the tensile deformation. As mentioned above, at the onset of instability, the material deforms with the eigenmode corresponding to the dominant stability condition. Under uniaxial tensile loading, the bulk material loses instability due to the vanishing of the tetragonal shear modulus $G' = (\bar{B}_{22} - \bar{B}_{23})/2$ whereas the vanishing of the Young's modulus $E_{[100]} = \frac{D_3}{\bar{B}_{22}\bar{B}_{33} - \bar{B}_{23}^2}$ is the reason for the elastic instability

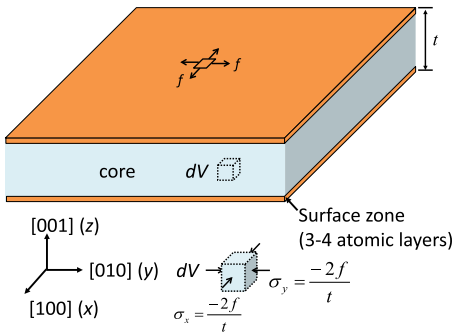

FIG. 5. Free-body diagram of an fcc metal (001) nanoplate with thickness t at equilibrium. At equilibrium, the tensile surface stress induces compressive stress components in the in-plane directions. The tensile surface-stress components in the x and y directions, respectively, balance the compressive stress components in the core in the x and y directions at equilibrium.

loss of the nanoplate. Consequently, the eigenmode of the nanoplate is not the same as that of the bulk. Specifically, the sudden change in the lateral strains of the bulk materials under the uniaxial stress is replaced by a smooth change. Therefore, due to surface stresses, the mechanical response of the nanoplate is significantly different from those of the bulk material in both the elastic regime and elastic instability regime. In the nanoplate, the elastic instability event occurs without a sudden change in lateral strains (phase transformation) and stress gradually decreases after the instability.

To provide more evidence to support our explanation, we conducted a simulation for the Au bulk under the multiaxial loading condition, i.e., the modeled nanoplate. Specifically, we imposed the above-described multiaxial stress condition on the Au bulk, where strain is applied along the x direction, a finite compressive stress equal to the magnitude induced by the surface stress is applied along the y direction, and a stress-free condition is applied along the z direction. Remarkably, the mechanical response of the modeled nanoplate and the nanoplate in both the elastic regime and elastic instability regime are almost the same (Fig. 2). The critical point for the modeled nanoplate is marked by a pair of blue arrows, and so Fig. 2 clearly demonstrates the significant effect that surface stress has on the mechanical response of the metal nanoplates.

We have verified that the elastic instability is a general result for metal nanoplates by investigating nanoplates with different potential models [18–20] with different materials such as Cu, Ag, Au, Ni, Pd, and Pt, and different temperatures ranging from 1 to 500 K. It is noted that the potentials of Foiles *et al.* [19] and Cai and Ye [18] have been rigorously evaluated with regards to elastic and defect properties, and are known to give good agreement with elastic constants while underestimating both the stacking fault and surface energies for fcc metals. To demonstrate that the EAM potentials we utilized do not impact the conclusions of the paper, we also show results using the EAM potential of Voter and Chen [20] for Au. The Voter-Chen potential was used due to its ability to accurately capture the stacking fault energies of Au accurately with respect to benchmark *ab initio* and experimental data (Table II). Specifically, the intrinsic stacking fault energy of the Voter-Chen potential for Au is 30.6 $\mathrm{mJ/m^2}$ which is very close

TABLE II. Comparison of surface properties of Au predicted by EAM potentials, DFT calculations, and experiment data. $\gamma_{(111)}$, $\gamma_{(100)}$, and $\gamma_{(110)}$ are the surface energy of the planes (111), (100), and (110), respectively; and γ_{isf} is the intrinsic stacking fault energy. The surface energy obtained by experiment in Ref. [45] is the average surface energy.

Property	Foiles *et al.* [19]	Cai and Ye [18]	Voter and Chen [20]	DFT	Experiment
$\gamma_{(111)}$ (mJ/m^2)	790	618	1030	1283 [44]	1500 [45]
$\gamma_{(100)}$ (mJ/m^2)	918	683	1180	1627 [44]	1500 [45]
$\gamma_{(110)}$ (mJ/m^2)	980	728	1395	1700 [44]	1500 [45]
γ_{isf} (mJ/m^2)	4.9	2.1	30.6	32.7 [46]	32 [47]

to that obtained by experiment, 32 mJ/m^2, and that predicted by DFT calculation, 32.7 mJ/m^2. The Voter-Chen potential also gives good predictions of the surface energies (Table II). The Voter-Chen potential reproduces the results discussed previously that the nanoplates fail via elastic instability; i.e., critical strains ε_I for elastic instability are smaller than the yield strains ε_Y as can be seen in Table III. Table III also lists ε_I and ε_Y for six different nanoplates. It is clear that for all cases, ε_I is always smaller than ε_Y.

We also discuss contrasts with metal nanowires, where elastic instability was also observed for symmetric (square or circular) cross sections [48]. However, the deformation of the nanoplate and the symmetric nanowires are significantly different. First, in the elastic regime, the nanowires contract along both the y and z directions; thus the Poisson's ratio is always positive, whereas a negative Poisson's ratio can be observed in the nanoplate. Second, the elastic instability event in the nanowires is a phase transformation, which is not observed for the nanoplate. Another important issue is the temperature effect. Elastic instability always occurs in the nanoplates at all temperatures (0–500 K) (see Fig. 6), whereas elastic instability can occur at low temperatures (lower than 10 K for the Au [100]/(001) square nanowire with the same potential model as in the present Au (001) nanoplate) for nanowires. Thus failure via elastic instability appears to be a common property for metal nanoplates, rather than the expected plastic yielding mechanism.

TABLE III. Metal (001) nanoplates with the same 23-layer thickness. For each metal, the first row and second row, respectively, present the results with the EAM potential developed by Foiles *et al.* [19] and the EAM potential developed by Cai and Ye [18]. For the case of Au, the third row is the results with the EAM potential developed by Voter and Chen [20]. In all cases, ε_Y is larger than ε_I.

Metal	σ_I (GPa)	ε_I	ε_Y
Au	2.277	0.0682	0.0809
	3.022	0.0775	0.0884
	4.158	0.0998	0.1139
Ag	4.852	0.0854	0.0946
	2.840	0.0757	0.0858
Cu	4.793	0.0783	0.0901
	4.063	0.0722	0.0815
Ni	9.469	0.0834	0.0925
	6.226	0.0739	0.0831
Pd	3.144	0.0694	0.0817
	4.717	0.0774	0.0871
Pt	1.844	0.0570	0.0693
	5.388	0.0774	0.0876

C. Ideal strength of metal nanoplates

We have established that under uniaxial stress, metal (001) nanoplates exhibit an intermediate mechanical regime between the elastic and plastic regimes, that of elastic instability. As a result, the relevant strength measure of the nanoplate is the ideal strength, rather than the yield strength. Interestingly, the ideal strength of the Au nanoplate with a thickness of 4.7 nm is 3.02 GPa, which is smaller than that of the bulk Au (4.38 GPa). We calculate the ideal strength of nanoplates with different thicknesses at 1 K and plot them in Fig. 7. Here, we observe the unexpected trend of "smaller is weaker." This observation is different from the common observation in nanoscale materials that "smaller is stronger" [49,50].

As the nanoplate fails by elastic instability, the maximum stress is the corresponding ideal strength. The ideal strength of the nanoplates (σ_{IP}) can be regarded as a summation of ideal strength of the core and the modification due to surface stresses.

$$\sigma_{IP} = \sigma_I^{\text{Core}} + \sigma_S, \tag{1}$$

where σ_I^{Core} is the strength of the core and σ_S is the contribution from the surface stress, which is the additional tensile stress needed to overcome the residual compressive stress in the core along the loading direction due to tensile surface stress. As mentioned earlier, the core is under a multiaxial stress

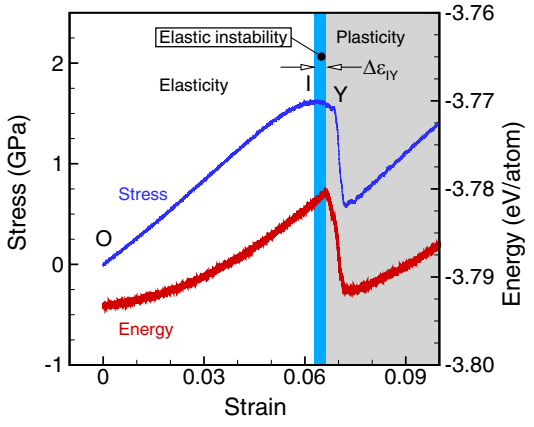

FIG. 6. Stress-strain and energy-strain curves of the Au (001) nanoplate with a thickness of 4.7 nm under uniaxial stress along the [100] direction at 500 K. The nanoplate experiences the elastic instability regime even at high temperatures.

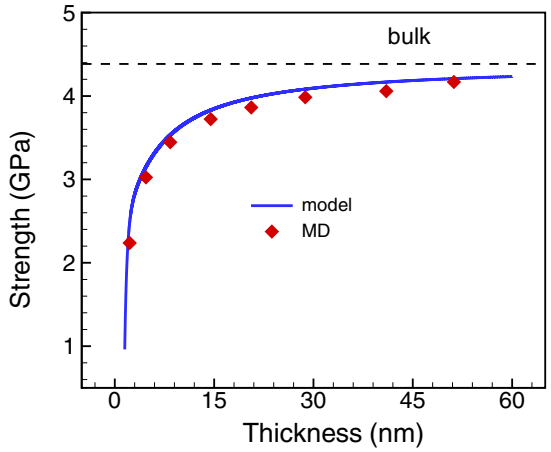

FIG. 7. Dependence of ideal strength of Au (001) nanoplate on thickness at 1 K. The trend "smaller is weaker" is observed. The model is in excellent agreement with the MD simulation result.

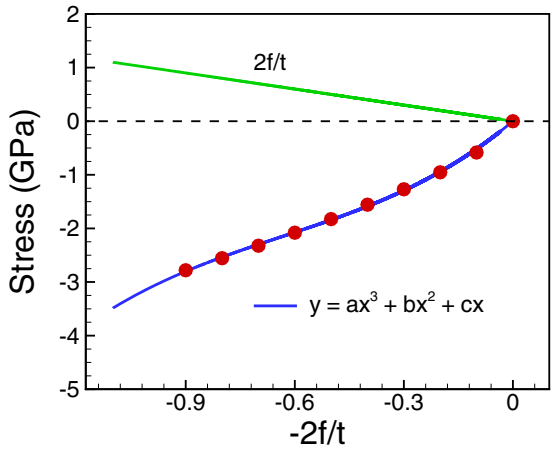

FIG. 8. The contribution of surface stress (green line, $2f/t$) and the compressive stress induced by surface stress on the ideal strength of the Au (001) nanoplate (red dots, blue fitting line). The compressive stress induced by surface-stress data are fitted to the function $y = F(x) = ax^3 + bx^2 + cx$, with $a = 2.841$, $b = 5.403$, and $c = 5.674$.

state, even though the nanoplate is subject to uniaxial stress: In addition to the applied stretch along the x direction, a compressive stress σ_a is induced along the y direction while the stress along the z direction becomes zero because of the free surface of the nanoplate along the z direction. The value of σ_a is dependent on the thickness t of the nanoplate and the orientation of the free surface. For an fcc (001) nanoplate with the surface stress f, σ_a can be obtained as [16]

$$\sigma_a = -\frac{2f}{t}. \tag{2}$$

Under the multiaxial loading condition, it is important to mention that the ideal strength σ_{IB} of the bulk material depends on the value of the applied stresses along the lateral directions [51]:

$$\sigma_{IB} = \sigma_{IB}^0 + F(\sigma_y), \tag{3}$$

where σ_{IB}^0 is the ideal strength of the bulk material under the uniaxial stress condition and $F(\sigma_y)$ captures the effect of the applied stress along the lateral direction on the ideal strength.

The strength of the core σ_I^{Core} can be obtained by using Eq. (3) with $\sigma_y = \sigma_a = -2f/t$:

$$\sigma_I^{\text{Core}} = \sigma_{IB}^0 + F\left(-\frac{2f}{t}\right). \tag{4}$$

For fcc (001) nanoplates, the residual compressive stress in the x direction is the same as that in the y direction, $-2f/t$; then the additional tensile stress needed to overcome the residual compressive stress is [16]

$$\sigma_S = \frac{2f}{t}. \tag{5}$$

Substituting Eqs. (4) and (5) into Eq. (1) yields

$$\sigma_{IP} = \sigma_{IB}^0 + F\left(-\frac{2f}{t}\right) + \frac{2f}{t}. \tag{6}$$

Prediction of the size-dependent strength based on Eq. (6) requires the term $F(-2f/t)$ to be determined. We follow an approach used previously [51] to obtain the function F. In particular, we first calculate the ideal strength σ_{IB} of the bulk fcc under the multiaxial stress condition in which strain is applied along the x direction, a finite compressive stress is applied along the y direction, and a stress-free condition is applied along the z direction. Various simulations with different values of σ_y from 0 to 0.9 GPa were conducted. The ideal strengths are obtained as the value when the bulk material loses its elastic stability. Then the change of F with respect to σ_y is calculated as the difference between the ideal strength of the bulk under the multiaxial stress condition and that of the bulk under uniaxial stress condition [Eq. (4)]. The data of F are fitted by the form $F(-2f/t) = F(x) = ax^3 + bx^2 + cx$ where we obtain $a = 2.841$, $b = 5.403$, and $c = 5.674$ (Fig. 8). Under this multiaxial stress condition, the ideal strength is significantly reduced with the applied stress along a lateral direction [51]. As the magnitude of stress along a lateral direction increases, the elastic instability occurs earlier, and consequently, the ideal strength is reduced.

We present in Fig. 7 a comparison between our ideal strength model in Eq. (6) and the direct atomistic simulations of the ideal strength of the Au nanoplates with different thicknesses at 1 K. As can be seen, the prediction of the model is in excellent agreement with the simulation results. We point out once again that the trend "smaller is weaker" is observed in the nanoplates. We repeated the simulations for other metals, namely Ag, Ni, Cu, Pd, and Pt, and the same behavior is observed.

Two terms in Eq. (6) can change the ideal strength of the nanoplate. For fcc metals, the surface stress is almost always tensile, and thus the term $2f/t$ tends to enhance the strength of the materials. On the other hand, the large tensile surface stress generates a large compressive stress in the core of the nanoplate. Therefore, in another way, surface stress changes the ideal strength of the nanoplate through the contribution to the ideal strength of the core. We plot the contributions of the two terms in Fig. 8. As can be seen, as the thickness decreases, the reduction by the term $F(-2f/t)$ is much greater than the

enhancement of the term $2f/t$; therefore, the net contribution from the two terms becomes a reduction, and the reduction increases as the thickness decreases. Consequently, the trend "smaller is weaker" is observed in the nanoplates.

IV. CONCLUSIONS

In summary, we performed atomistic simulations to investigate the mechanical response of metal (001) nanoplates under uniaxial stress along the [100] direction. Our simulations show that the nanoplates usually fail due to elastic instability instead of dislocation-mediated plasticity as typically observed. At the onset of the elastic instability regime, the nanoplates fail homogeneously and globally. Such homogeneous and global deformation can be observed for all nanoplates at considered temperatures ranging from 0 to 500 K. Furthermore, the ideal strengths of the nanoplates decrease with decreasing plate thickness, resulting in an unusual "smaller is weaker" trend. This occurs due to competing effects engendered by the surface stress. Specifically, tensile surface stresses in thinner (001) nanoplates generate residual compressive stress along the loading direction in the cores so that additional tensile stress is needed to overcome the residual stress, which enhances the strength as described in Eq. (1). However, the tensile surface stress in thinner nanoplates also generates a large compressive stress in the core of the nanoplate, causing elastic instability to occur sooner, thus reducing the ideal strength. The latter effect, i.e., the reduction of ideal strength, is found to be much more significant than the first effect, resulting in the observed "smaller is weaker" strength trend in the metal nanoplates. These results were accurately captured using a simple surface-stress-based analytic model for the ideal strength of the nanoplates.

Overall, while the elastic stiffness of metal nanostructures has been shown to both increase and decrease relative to the bulk value [17,52] this work has reported the unexpected "smaller is weaker" phenomenon, where many other experimental and theoretical studies of metal nanostructures have reported enhanced strength with decreasing size. For example, while surface stress enhances the strength of nanowires such as fcc metal nanowires [53] and Si nanowires [54], the surface stress in this study reduces the ideal strength of metal nanoplates. This represents an interesting case study to demonstrate that surface effects can cause significant, and unexpected behaviors in mechanical response of nanomaterials.

ACKNOWLEDGMENTS

We gratefully acknowledge the support from the ICT R&D Program (Grant No. R0190-15-2012) of the Institute for Information Communications Technology Promotion (IITP) and from the Mid-Career Researcher Support Program (Grant No. 2014R1A2A2A09052374) of the National Research Foundation (NRF), both of which are funded by the MSIP of Korea. We also acknowledge with gratitude the PLSI supercomputing resources of the KISTI and the UNIST Supercomputing Center. H.S.P. acknowledges the support of the Mechanical Engineering department at Boston University.

APPENDIX: ELASTIC STABILITY CONDITIONS FOR THE METAL NANOPLATES UNDER UNIAXIAL STRESS ALONG THE [100] DIRECTION

The elastic stability theory [13] states that a material is stable at the current state if the change in the internal energy δU is larger than the change in the work done by external loading δW for *all possible, arbitrary virtual infinitesimal deformation*:

$$\delta U - \delta W > 0. \tag{A1}$$

This condition is simplified to $\det|\bar{\mathbf{B}}| > 0$ where $\bar{\mathbf{B}} = 1/2(\mathbf{B} + \mathbf{B}^T)$ and $\mathbf{B}$ is the elastic stiffness matrix that is the combination of elastic moduli $\mathbf{C}$ and external loading τ_{ij} [26]:

$$B_{ijkl} = C_{ijkl} + \tfrac{1}{2}(\delta_{ik}\tau_{jl} + \delta_{jk}\tau_{il} + \delta_{il}\tau_{jk} + \delta_{jl}\tau_{ik} - 2\delta_{kl}\tau_{ij}), \tag{A2}$$

where δ_{ij} is the Kronecker delta. The elastic moduli at the deformed configuration x is defined as

$$C_{ij} = \frac{1}{V}\frac{\partial^2 U}{\partial E_{ij}\partial E_{ij}}\bigg|_{X,E'}, \tag{A3}$$

where V is the volume of the system, U is the internal energy, and E_{ij} is the Lagrangian strain. The derivative in Eq. (A3) is calculated at the state x with all other strains $E' \neq E$ held constant. It is noted that the elastic stiffness tensor matrix B was originally introduced by Wallace [28]. In the study of elastic instability of materials, the elastic stiffness matrix is usually calculated at each deformed configuration for checking the stability condition [26,55]. It is noted that the elastic stiffness matrix in Eq. (A2) can be obtained as an expansion of the applied strain tensor, elastic constants, and third-order elastic constants at the undeformed configuration [56]. In this study, the elastic stiffness matrix is calculated at each deformed configuration. When $\det|\bar{\mathbf{B}}| = 0$, the material becomes unstable and deforms with an eigenstate. One can obtain the eigenstate by solving an eigenvalue problem: $(\bar{\mathbf{B}} - \lambda\mathbf{I})\mathbf{x} = \mathbf{0}$. It is important to note that the deformation mode at onset of instability can be homogeneous. For cubic materials under uniaxial stress τ along the [100] direction, $\bar{\mathbf{B}}$ has six independent components: $\bar{B}_{11} = C_{11} + \tau$; $\bar{B}_{22} = \bar{B}_{33} = C_{22}$; $\bar{B}_{12} = \bar{B}_{13} = C_{12} - \tau/2$; $\bar{B}_{23} = C_{23}$; $\bar{B}_{44} = C_{44}$; $\bar{B}_{55} = \bar{B}_{66} = C_{55} + \tau/2$. The condition $\det|\bar{\mathbf{B}}| > 0$ can be further simplified to the following conditions in Voigt notation:

$$\bar{B}_{22} + \bar{B}_{23} - 2\bar{B}_{12}^2/\bar{B}_{11} > 0 \text{ or } (C_{22} + C_{23}) - 2(C_{12} - \tau/2)^2/(C_{11} + \tau) > 0, \tag{A4}$$

$$\bar{B}_{22} - \bar{B}_{23} > 0 \text{ or } C_{22} - C_{23} > 0, \tag{A5}$$

$$\bar{B}_{44} > 0 \text{ or } C_{44} > 0, \tag{A6}$$

$$\bar{B}_{55} > 0 \text{ or } C_{55} + \tau/2 > 0. \tag{A7}$$

When one of the above conditions vanishes, the cubic material loses its elastic stability. Each vanishing corresponds

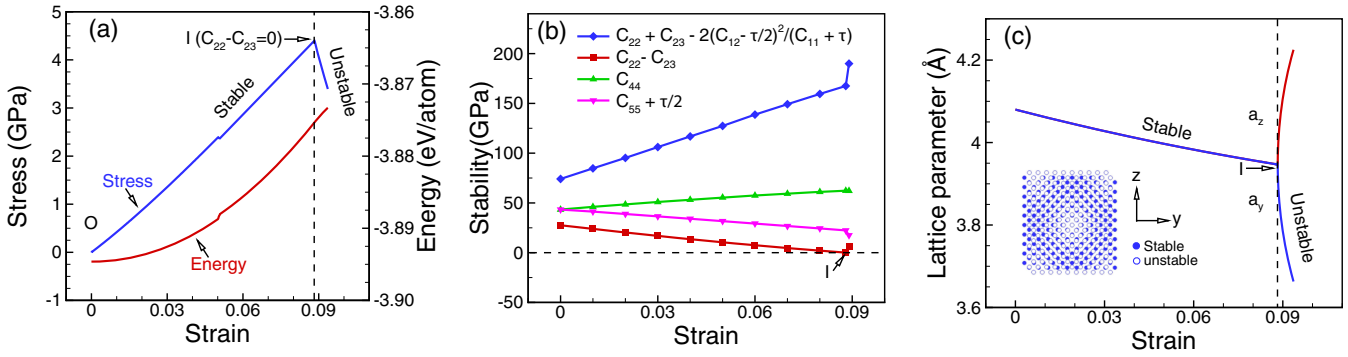

FIG. 9. Mechanical response of fcc Au single crystal under uniaxial tension along the [100] direction. (a) Stress-strain and energy-strain curves, (b) the change of the elastic stability terms with applied strain, and (c) The change of the lateral lattice parameters with applied strain. The material fails at the strain of 0.088. At this point, the stress is maximum. While the stress decreases after the critical strain, the energy still increases. The failure deformation is homogeneous.

to an eigensolution:

$$(2\bar{B}_{12},-\bar{B}_{11},-\bar{B}_{11},0,0,0) \text{ when } (C_{22}+C_{23})-2(C_{12}-\tau/2)^2/(C_{11}+\tau)>0, \quad \text{(A8)}$$

$$(0,-1,1,0,0,0) \text{ when } C_{22}-C_{23}>0, \quad \text{(A9)}$$

$$(0,0,0,1,0,0) \text{ when } C_{44}>0, \quad \text{(A10)}$$

$$(0,0,0,0,1,0) \text{ or } (0,0,0,0,0,1) \text{ when } C_{55}+\tau/2>0. \quad \text{(A11)}$$

Figure 9(a) shows the stress-strain curves of Au bulk under uniaxial tensile loading along the [100] direction. The MD simulation was performed at 1 K. The EAM potential by Cai and Ye [18] is used to describe the interaction between Au atoms. Under an applied strain, the stress increases gradually and drops after reaching a maximum value of 4.38 GPa and the corresponding strain is 0.088. One of the stability conditions, i.e., $C_{22}-C_{23}>0$, vanishes exactly at the maximum stress. We also plot the changes of lateral lattice parameter a_y and a_z in Fig. 9(c). Before the critical strain, when strain increases, the lateral lattice parameters decrease gradually with the same amount, so the phase of the material is tetragonal. However, at the onset of instability; i.e., when the stability condition $C_{22}-C_{23}>0$ vanishes, there is large contraction along the y direction whereas there is large expansion along the z direction, so the phase of the material is orthorhombic. In other words, we can see a phase transformation in the material from tetragonal to orthorhombic at the maximum stress. The phase transformation is homogeneous across the structure. This failure mode is the same as the eigensolution predicted by the theory [33,34]. It is worth mentioning that as in the case of the nanoplate, while the stress drops due to the elastic instability, energy still increases as can be seen in Fig. 9(a).

For the case of metal (001) nanoplates under the uniaxial stress condition along the [100] direction, the elastic stiffness matrix has nine components instead of six as in the case of the bulk counterpart: $\bar{B}_{11}$, $\bar{B}_{22}$, $\bar{B}_{33}$, $\bar{B}_{12}$, $\bar{B}_{13}$, $\bar{B}_{23}$, $\bar{B}_{44}$, $\bar{B}_{55}$, and $\bar{B}_{66}$. Then the necessary and sufficient conditions for the elastic stability of the material become the following:

$$D_1=\bar{B}_{11}>0, \quad \text{(A12)}$$

$$D_2=\begin{vmatrix}\bar{B}_{11} & \bar{B}_{12}\\ \bar{B}_{12} & \bar{B}_{22}\end{vmatrix}>0, \quad \text{(A13)}$$

$$D_3=\begin{vmatrix}\bar{B}_{11} & \bar{B}_{12} & \bar{B}_{13}\\ \bar{B}_{12} & \bar{B}_{22} & \bar{B}_{23}\\ \bar{B}_{13} & \bar{B}_{23} & \bar{B}_{33}\end{vmatrix}>0, \quad \text{(A14)}$$

$$D_4=\bar{B}_{44}>0, \quad \text{(A15)}$$

$$D_5=\bar{B}_{55}>0, \quad \text{(A16)}$$

$$D_6=\bar{B}_{66}>0. \quad \text{(A17)}$$

Note that the effective Young's modulus along the [100] direction for an orthorhombic crystal is given as

$$E_{[100]}=\frac{\bar{B}_{11}\bar{B}_{22}\bar{B}_{33}+2\bar{B}_{23}\bar{B}_{12}\bar{B}_{13}-\bar{B}_{11}\bar{B}_{23}^2-\bar{B}_{22}\bar{B}_{13}^2-\bar{B}_{33}\bar{B}_{12}^2}{\bar{B}_{22}\bar{B}_{33}-\bar{B}_{23}^2}=\frac{D_3}{\bar{B}_{22}\bar{B}_{33}-\bar{B}_{23}^2}. \quad \text{(A18)}$$

Equation (A18) shows that the vanishing of the elastic moduli combination D_3 corresponds to the vanishing of the effective Young's modulus along the loading direction.

[1] K. Gall, J. Diao, and M. L. Dunn, Nano Lett. **4**, 2431 (2004).
[2] J. R. Greer and J. T. M. De Hosson, Prog. Mater. Sci. **56**, 654 (2011).
[3] B. Wu, A. Heidelberg, and J. J. Boland, Nat. Mater. **4**, 525 (2005).
[4] H. D. Espinosa, B. C. Prorok, and B. Peng, J. Mech. Phys. Solids **52**, 667 (2004).

[5] A. Rinaldi, P. Peralta, C. Friesen, and K. Sieradzki, Acta Mater. **56**, 511 (2008).
[6] O. Torrents Abad, J. M. Wheeler, J. Michler, A. S. Schneider, and E. Arzt, Acta Mater. **103**, 483 (2016).
[7] Y. Zhu, Q. Qin, F. Xu, F. Fan, Y. Ding, T. Zhang, B. J. Wiley, and Z. L. Wang, Phys. Rev. B **85**, 045443 (2012).
[8] J. R. Greer, W. C. Oliver, and W. D. Nix, Acta Mater. **53**, 1821 (2005).
[9] F. Milstein, Phys. Rev. B **3**, 1130 (1971).
[10] H. Wang and M. Li, J. Phys.: Condens. Matter **22**, 295405 (2010).
[11] M. Born, Math. Proc. Cambridge Philos. Soc. **36**, 160 (1940).
[12] R. Hill, Math. Proc. Cambridge Philos. Soc. **77**, 225 (1975).
[13] R. Hill and F. Milstein, Phys. Rev. B **15**, 3087 (1977).
[14] Q. G. Zhang, B. Y. Cao, X. Zhang, M. Fujii, and K. Takahashi, Phys. Rev. B **74**, 134109 (2006).
[15] D. T. Ho, H. Kim, S.-Y. Kwon, and S. Y. Kim, Phys. Status Solidi B **252**, 1492 (2015).
[16] D. T. Ho, S.-D. Park, S.-Y. Kwon, K. Park, and S. Y. Kim, Nat. Commun. **5**, 3255 (2014).
[17] H. Liang, M. Upmanyu, and H. Huang, Phys. Rev. B **71**, 241403 (2005).
[18] J. Cai and Y. Y. Ye, Phys. Rev. B **54**, 8398 (1996).
[19] S. M. Foiles, M. I. Baskes, and M. S. Daw, Phys. Rev. B **33**, 7983 (1986).
[20] A. F. Voter and S. P. Chen, in *Characterization of Defects in Materials*, Materials Research Society Symposium Proceedings No. 82 (Materials Research Society, Pittsburgh, 1987), p. 175.
[21] S. Plimpton, J. Comput. Phys. **117**, 1 (1995).
[22] A. Stukowski, Modell. Simul. Mater. Sci. Eng. **18**, 015012 (2010).
[23] Z. X. Wu, Y. W. Zhang, M. H. Jhon, J. R. Greer, and D. J. Srolovitz, Acta Mater. **61**, 1831 (2013).
[24] H. S. Park, K. Gall, and J. A. Zimmerman, J. Mech. Phys. Solids **54**, 1862 (2006).
[25] C. R. Weinberger and W. Cai, J. Mater. Chem. **22**, 3277 (2012).
[26] J. Wang, J. Li, S. Yip, S. Phillpot, and D. Wolf, Phys. Rev. B **52**, 12627 (1995).
[27] J. W. Morris and C. R. Krenn, Philos. Mag. A **80**, 2827 (2000).
[28] D. C. Wallace, *Thermodynamics of Crystals* (John Wiley & Sons, New York, 1972).
[29] J. Li, T. Zhu, K. J. Van Vliet, S. Yip, and S. Suresh, Nature **418**, 307 (2002).
[30] T. Zhu, J. Li, K. J. Van Vliet, S. Ogata, S. Yip, and S. Suresh, J. Mech. Phys. Solids **52**, 691 (2004).
[31] T. Kitamura, Y. Umeno, and R. Fushino, Mater. Sci. Eng.: A **379**, 229 (2004).
[32] T. Kitamura, Y. Umeno, and N. Tsuji, Comput. Mater. Sci. **29**, 499 (2004).
[33] F. Milstein, J. Marschall, and H. E. Fang, Phys. Rev. Lett. **74**, 2977 (1995).
[34] F. Milstein and B. Farber, Phys. Rev. Lett. **44**, 277 (1980).
[35] H. S. Park, K. Gall, and J. A. Zimmerman, Phys. Rev. Lett. **95**, 255504 (2005).
[36] W. Liang, M. Zhou, and F. Ke, Nano Lett. **5**, 2039 (2005).
[37] R. C. Cammarata, Prog. Surf. Sci. **46**, 1 (1994).
[38] V. B. Shenoy, Phys. Rev. B **71**, 094104 (2005).
[39] R. Dingreville and J. Qu, Acta Mater. **55**, 141 (2007).
[40] D. T. Ho, S.-D. Park, H. Lee, S.-Y. Kwon, and S. Y. Kim, Europhys. Lett. **106**, 36001 (2014).
[41] R. J. Needs, M. J. Godfrey, and M. Mansfield, Surf. Sci. **242**, 215 (1991).
[42] J. Diao, K. Gall, and M. L. Dunn, J. Mech. Phys. Solids **52**, 1935 (2004).
[43] J. Diao, K. Gall, and M. L. Dunn, Phys. Rev. B **70**, 075413 (2004).
[44] L. Vitos, A. V. Ruban, H. L. Skriver, and J. Kollár, Surf. Sci. **411**, 186 (1998).
[45] W. R. Tyson and W. A. Miller, Surf. Sci. **62**, 267 (1977).
[46] R. Li, S. Lu, D. Kim, S. Schönecker, J. Zhao, S. K. Kwon, and L. Vitos, J. Phys.: Condens. Matter **28**, 395001 (2016).
[47] M. L. Jenkins, Philos. Mag. **26**, 747 (1972).
[48] D. T. Ho, Y. Im, S.-Y. Kwon, Y. Y. Earmme, and S. Y. Kim, Sci. Rep. **5**, 11050 (2015).
[49] M. D. Uchic, D. M. Dimiduk, J. N. Florando, and W. D. Nix, Science **305**, 986 (2004).
[50] G. Ouyang, G. Yang, C. Sun, and W. Zhu, Small **4**, 1359 (2008).
[51] D. T. Ho, S.-D. Park, S.-Y. Kwon, T.-S. Han, and S. Y. Kim, Europhys. Lett. **111**, 26005 (2015).
[52] H. S. Park, W. Cai, H. D. Espinosa, and H. Huang, MRS Bull. **34**, 178 (2009).
[53] J.-H. Seo, H. S. Park, Y. Yoo, T.-Y. Seong, J. Li, J.-P. Ahn, B. Kim, and I.-S. Choi, Nano Lett. **13**, 5112 (2013).
[54] Y. Zhu, F. Xu, Q. Qin, W. Y. Fung, and W. Lu, Nano Lett. **9**, 3934 (2009).
[55] I. S. Winter, M. de Jong, M. Asta, and D. C. Chrzan, Phys. Rev. Mater. **1**, 030601 (2017).
[56] M. de Jong, I. Winter, D. C. Chrzan, and M. Asta, Phys. Rev. B **96**, 014105 (2017).